Editors' Suggestion

Quantum oscillations in the centrosymmetric skyrmion-hosting magnet $GdRu_2Si_2$

N. Matsuyama,[1,*] T. Nomura,[1] S. Imajo,[1] T. Nomoto,[2,3] R. Arita,[2,4] K. Sudo,[5] M. Kimata,[5] N. D. Khanh,[4,6] R. Takagi,[3,4,6,7] Y. Tokura,[4,6,8] S. Seki,[4,6,7] K. Kindo,[1] and Y. Kohama[1]

[1]*Institute for Solid State Physics, University of Tokyo, Kashiwa, Chiba 277-8581, Japan*
[2]*Research Center for Advanced Science and Technology, University of Tokyo, Meguro-ku, Tokyo 153-8904, Japan*
[3]*PRESTO, Japan Science and Technology Agency, Kawaguchi, Saitama 332-0012, Japan*
[4]*RIKEN Center for Emergent Matter Science, Wako, Saitama 351-0198, Japan*
[5]*Institute for Materials Research, Tohoku University, Sendai, Miyagi 980-8577, Japan*
[6]*Department of Applied Physics, University of Tokyo, Bunkyo-ku, Tokyo 113-8656, Japan*
[7]*Institute of Engineering Innovation, University of Tokyo, Tokyo 113-0032, Japan*
[8]*Tokyo College, University of Tokyo, Bunkyo-ku, Tokyo 113-8656, Japan*

(Received 26 December 2022; accepted 6 March 2023; published 21 March 2023)

We have performed magnetic torque and resistivity measurements on the centrosymmetric skyrmion host $GdRu_2Si_2$, in which the dominant magnetic interaction leading to skyrmion formation is under debate. We observe both the de Haas–van Alphen and Shubnikov–de Haas oscillations in the forced ferromagnetic phase. The angular dependence of the quantum oscillation frequencies can be reproduced by an *ab initio* calculation. The de Haas–van Alphen oscillation is also observed in the double-**Q** phase with a frequency different from that in the forced ferromagnetic phase, indicating a Fermi surface reconstruction due to the coupling between localized spins and conduction electrons. Based on these experimental findings, the magnetic interactions in this system are discussed.

DOI: 10.1103/PhysRevB.107.104421

I. INTRODUCTION

The magnetic skyrmion has been of great interest since its discovery because of its topological characteristics and thus its potential applications in a next-generation magnetic memory and logic device. In the early stages of the research, skyrmions were found in noncentrosymmetric systems, where the competition between the ferromagnetic exchange and Dzyaloshinskii-Moriya (DM) interaction favors helical spin structures [1–8]. Recently, a skyrmion lattice (SkL) phase was even discovered in several centrosymmetric rare-earth alloys that lack the DM interaction [9–12].

$GdRu_2Si_2$ is one such centrosymmetric skyrmion host and has the shortest-period SkL ever found [11]. It crystallizes in the $ThCr_2Si_2$-type body-centered tetragonal structure with space group $I4/mmm$ [Fig. 1(a)]. Gd^{3+} ions ($S = 7/2, L = 0$) are the source of magnetism in this material and form a square lattice within the *ab* plane. The local moments of Gd^{3+} show long-range magnetic ordering at $T_N \sim 46$ K [13–15] with various field-induced phases [16,17]. As shown in the phase diagram [Fig. 1(b)], three magnetic phases (phases I–III) appear below T_N with a field along the *c* axis. These phases are characterized by different combinations of two orthogonally modulated spin helices with incommensurate wave vectors $\mathbf{Q}_1 \sim (0.22, 0, 0)$ and $\mathbf{Q}_2 \sim (0, 0.22, 0)$ [Fig. 1(c)]: Phase I is a superposition of sinusoidal and proper-screw spin helices, and phase III is described by two sinusoidal spin modulations, both of which are viewed as meron-antimeron lattice states with different patterns [11,18,19]. Phase II is the square SkL state with two proper-screw spin structures. Above 10 T, in the forced ferromagnetic (FF) phase, the magnetization saturates at $7\mu_B$ per Gd^{3+}.

The skyrmion stabilization mechanism for this material is still under debate. In the centrosymmetric crystal structure, the conventional mechanism based on the DM interaction is forbidden. Incommensurate magnetic modulations in rare-earth intermetallics are often brought about by the indirect exchange interaction mediated by conduction electrons, the so-called Ruderman-Kittel-Kasuya-Yosida (RKKY) interaction [20]. Indeed, the coupling between conduction electrons and localized magnetic moments was experimentally confirmed in $GdRu_2Si_2$ by a real-space observation using the scanning tunneling microscope (STM) technique [21]. Theoretically, several spin models based on the anisotropic exchange interactions [22,23], the RKKY interaction [24–26], and the multiple-spin interactions mediated by itinerant electrons [27–32] have succeeded in reproducing the SkL state in centrosymmetric systems. As for the microscopic origin to stabilize the fundamental helical modulation, there are two different interpretations proposed by first-principles calculations. One suggests that the RKKY interaction enhanced by Fermi surface nesting stabilizes the zero-field helical modulation [33], while the other proposes competition between ferromagnetic interaction in the Gd $5d$ channel and antiferromagnetic interaction in the Gd $4f$ channel, namely, the interorbital frustration plays a crucial role [34]. In order to discuss the possible origin of the helical modulation in this

*matsuyama@issp.u-tokyo.ac.jp

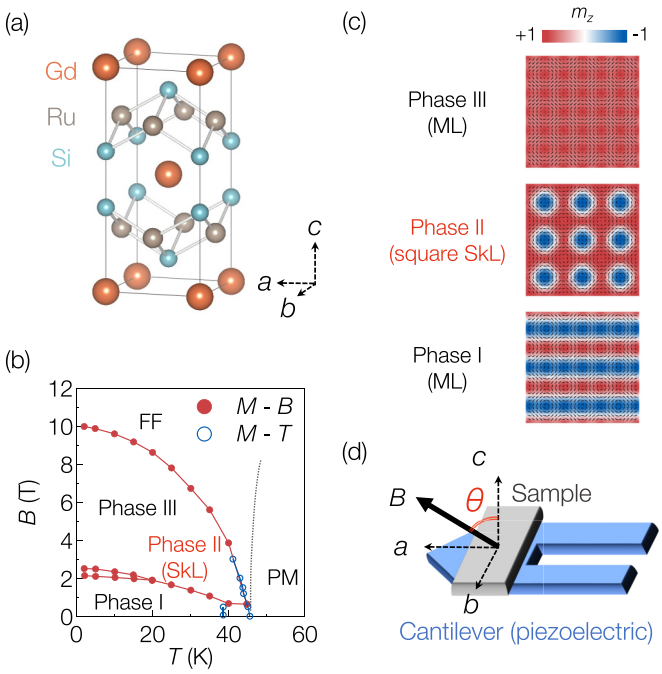

FIG. 1. (a) Crystal structure of $GdRu_2Si_2$ drawn by VESTA [35]. (b) B-T phase diagram for $B \parallel c$ axis [11]. (c) Magnetic structures in phases I–III. (d) Schematic illustration of the experimental condition. The sample was set on the piezoelectric cantilever, and the magnetic field was rotated in the ac plane. The angle θ is defined as the polar angle from the c axis.

centrosymmetric f-electron system, the electronic band structure of $GdRu_2Si_2$, which reflects how the f and conduction electrons interact with each other and contribute to the magnetic structures, needs to be clarified.

Here, we perform magnetic torque and resistivity measurements under high magnetic fields and at low temperatures to reveal the electronic structure of $GdRu_2Si_2$ through the de Haas–van Alphen (dHvA) and Shubnikov–de Haas (SdH) oscillations. The angular dependence of the dHvA oscillation frequency in the FF phase agrees with the *ab initio* calculation. Furthermore, Fermi surface reconstruction from phase III to the FF phase is observed, which indicates coupling between conduction electrons and localized spins. While the plausibility of the interorbital frustration mechanism should be investigated separately, these experimental findings suggest that the RKKY interaction is relevant to understand the helical magnetism and skyrmion formation in this system.

II. METHODS

High-quality single crystals were grown using the floating zone method under an Ar gas flow [11]. Several pieces of the sample with a residual resistivity ratio in the range of 50 to 100 were used in this research.

The angular dependence of the magnetic torque τ was investigated with a two-axis rotator up to 18 T using a superconducting magnet at the Institute for Materials Research (IMR), Tohoku University, and with a single-axis plastic rotator up to 58 T using a nondestructive pulsed magnet at the Institute for Solid State Physics, University of Tokyo. For both measurements, we utilized a commercial piezoelectric cantilever [36,37]. A tiny single crystal with a size of $\sim 200 \times 100 \times 30\,\mu m^3$ was mounted on top of the cantilever [Fig. 1(d)]. Magnetic torque τ, defined as the cross product of magnetization and magnetic fields ($\boldsymbol{\tau} = \boldsymbol{M} \times \boldsymbol{H}$), was measured as the change in the resistance of the piezoelectric cantilever.

The resistivity ρ of $GdRu_2Si_2$ was measured using the four-probe method with the current along the ab plane. The angular dependence of ρ was also measured with the two-axis rotator up to 18 T at IMR, Tohoku University. The field direction was rotated in the ac plane, and the field angle θ was defined as the relative angle from the c axis [Fig. 1(d)].

We compared the experimental data with the calculated electronic band structures. The calculation details are as follows: First, we performed spin density functional theory calculations based on the projector augmented wave scheme implemented in the Vienna Ab initio Simulation Package (VASP) [38,39]. Here, we employed the Perdew-Burke-Ernzerhof exchange-correlation functional [40] and assumed the collinear ferromagnetic order. The strong interactions in $4f$ orbitals of Gd were taken into account by the DFT + U method, where we set $U = 6.7$ eV and $J = 0.7$ eV. Then, we constructed the tight-binding model based on the Wannier function via the WANNIER90 code [41,42] and interpolated energy eigenvalues on a dense k grid of $51 \times 51 \times 51$. Finally, we calculated the dHvA frequencies using the SKEAF code [43].

III. RESULTS

A. Magnetic torque and magnetoresistance for $B \parallel c$

Figures 2(a) and 2(b) show the field dependences of τ with the field 2° away from the c axis and ρ for $B \parallel c$. These data are obtained at 1.3 K. Magnetization M at 5 K reported in Ref. [11] is shown for comparison [Fig. 2(c)]. All three quantities show several anomalies under magnetic fields corresponding to magnetic phase transitions. Below 2.0 T (phase I), magnetization and resistivity increase almost linearly, while magnetic torque shows a nearly quadratic change ($\boldsymbol{\tau} = \boldsymbol{M} \times \boldsymbol{H} \propto \boldsymbol{H}^2$). The magnetization shows a steplike structure in phase II (SkL phase; $2.0 < B < 2.7$ T), which is observed as a dip in magnetic torque and a hump in resistivity. The hump structures in the longitudinal and Hall resistivities of $GdRu_2Si_2$ have been reported within this field range [11]. The dip in magnetic torque suggests a drastic change in the magnetic anisotropy in phase II related to the SkL formation. In phase III, magnetization exhibits a sublinear increase and saturates at 10 T. With increasing magnetic field, magnetic torque shows a nonlinear increase up to the saturation, which may reflect the sublinear increase of the magnetization. The resistivity shows a broad peak and decreases towards saturation. The decrease in resistivity can be attributed to the suppression of spin fluctuations at high magnetic fields [17].

Quantum oscillations are observed in both magnetic torque (dHvA) and resistivity (SdH) in the FF phase ($B >$ 10 T), as shown in the insets of Figs. 2(a) and 2(b), respectively. Figures 3(a) and 3(b) show the oscillatory com-

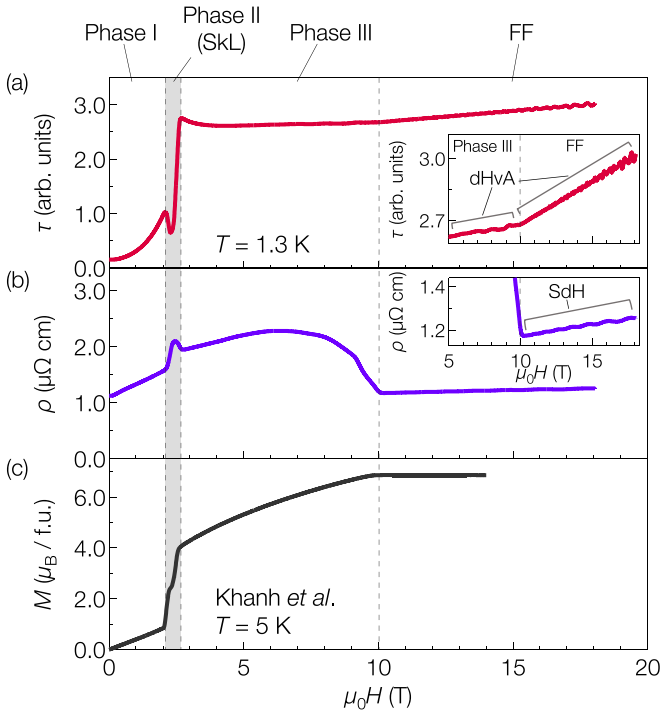

FIG. 2. Field dependence of (a) magnetic torque ($\theta = 2°$), (b) resistivity ($B \parallel c$) at $T = 1.3$ K, and (c) magnetization ($B \parallel c$) at $T = 5$ K [11] for $GdRu_2Si_2$. Observed quantum oscillations are highlighted in the insets.

ponents of magnetic torque and magnetoresistance at various temperatures as a function of inverse fields. The oscillatory components of the observed quantum oscillations are obtained by subtracting the smooth background deduced from a cubic polynomial fit. The fast Fourier transform (FFT) spectra of the dHvA and SdH oscillations are shown in Figs. 3(d) and 3(e), respectively. The FFT spectrum of the dHvA oscillations in the FF phase shows three main peaks, $F_1 = 563$ T, $F_2 = 763$ T, $F_3 = 1160$ T, and additional small peaks in the higher-frequency region, some of which are harmonics of the main peaks [Fig. 3(d)]. In contrast to the dHvA oscillations, the SdH oscillation consists of one predominant frequency, $F_S = 176$ T [Fig. 3(e)]. The peaks observed in the dHvA oscillations are seen as tiny peaks, as indicated by arrows. According to the Onsager relation $F = (\hbar/2\pi e)S_F$, where S_F is a cross-sectional area in momentum space, assuming a circular cross section $S_F = \pi k_F^2$ (k_F is the Fermi wave vector), one can estimate k_F corresponding to the observed frequency. The quantum oscillation frequencies and estimated Fermi wave vectors for $B \parallel c$ are listed in Table I.

We analyze the quantum oscillations of magnetic torque and resistivity using the Lifshitz-Kosevich (LK) formula, which is expressed as

$$\Delta\tau = C\sum_{p=1}^{\infty} B^{3/2} R_T R_D \sin\left[2\pi\left(\frac{F}{B} - \frac{1}{2}\right) + \Phi\right],$$

$$\Delta\rho/\rho_0 = C\sum_{p=1}^{\infty} B^{1/2} R_T R_D \cos\left[2\pi\left(\frac{F}{B} - \frac{1}{2}\right) + \Phi\right],$$

where C is a constant [44]. The Landau-level broadening caused by temperature and impurity scattering is represented by the damping factors $R_T = (K\mu/B)/[\sinh(K\mu T/B)]$ and $R_D = \exp(-K\mu T_D/B)$, respectively, with $K = (2\pi^2 m_0 k_B)/(e\hbar)$ and $\mu = m^*/m_0$, where k_B, m^*, and T_D represent the Boltzmann constant, the effective cyclotron mass, and Dingle temperature. T_D is related to the impurity scattering rate, and the corresponding scattering time τ_q can be deduced by $\tau_q = \hbar/(2\pi k_B T_D)$. The phase factor Φ derives from the dimensionality of the Fermi surface, Zeeman splitting, and Berry phase [45]. The observation of the quantum limits is often necessary for the precise determination of Φ, which is not achieved in this research. By fitting R_T and R_D to the temperature [insets of Figs. 3(d) and 3(e)] and field dependence of the FFT amplitude, we calculated m^*, T_D, τ_q, and mean-free path $l_q = v_F \cdot \tau_q = \hbar^2 k_F/(2\pi k_B m^* T_D)$ ($v_F = \hbar k_F/m^*$ is the Fermi velocity), as summarized in Table I.

The dHvA oscillation is observed in the high-field region of phase III ($6.0 < B < 10$ T) as well. The oscillatory components and their FFT spectra are shown in Figs. 3(c) and 3(f), respectively. The main peak is located at 73 T, which is roughly one order of magnitude smaller than the dHvA frequencies observed in the FF phase. The fit to the LK formula yields $m^* \sim 0.36 m_0$ [inset of Fig. 3(f)], and $T_D \sim 5.3$ K. τ_q and l_q are estimated as 0.23 ps and 35 nm.

B. Angular dependence

Next, the angular dependences of the magnetoresistance and magnetic torque are addressed. Figures 4(a) and 4(b) show the angular dependences of the magnetic torque and magnetoresistance at $T = 1.3$ K. The torque scaled by $\sin 2\theta$ is shown to magnify the torque signal around $B \parallel a$ and c, and the saturation fields are highlighted by dotted lines. For some angle θ and field ranges, we omit the torque data which

TABLE I. Oscillation frequency F, Fermi wave vector k_F, effective mass m^*/m_0, Dingle temperature T_D, scattering time τ_q, and mean free path l_q for each dHvA and SdH oscillation observed in the experiment for $GdRu_2Si_2$ ($B \parallel c$).

	Branch	F (T)	k_F (Å^{-1})	m^*/m_0	T_D (K)	τ_q (ps)	l_q (nm)
dHvA (FF phase)	F_1	563	0.13	0.30	15	0.081	40
	F_2	763	0.15	0.55	6.8	0.18	57
	F_3	1160	0.19	0.59	7.5	0.16	59
SdH (FF phase)	F_S	176	0.073	0.36	9.2	0.13	30
dHvA (phase III)	F_{PhaseIII}	73	0.047	0.36	1.3	0.23	35

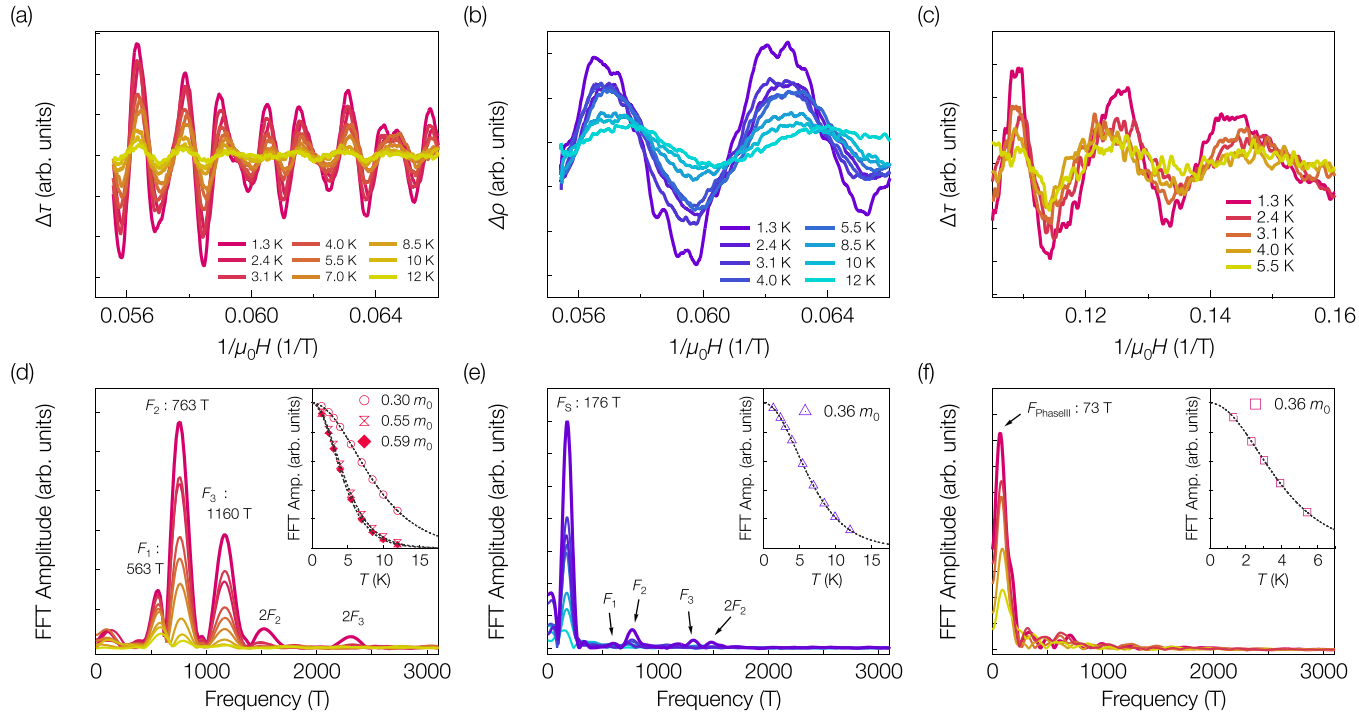

FIG. 3. Temperature dependence of oscillating components (top) and FFT spectra (bottom) of the observed dHvA (left) and SdH (middle) oscillations in the FF phase and dHvA oscillations in phase III (right). The field angles for dHvA and SdH experiments are $\theta = 2^\circ$ and $\theta = 0^\circ$ ($B \parallel c$), respectively.

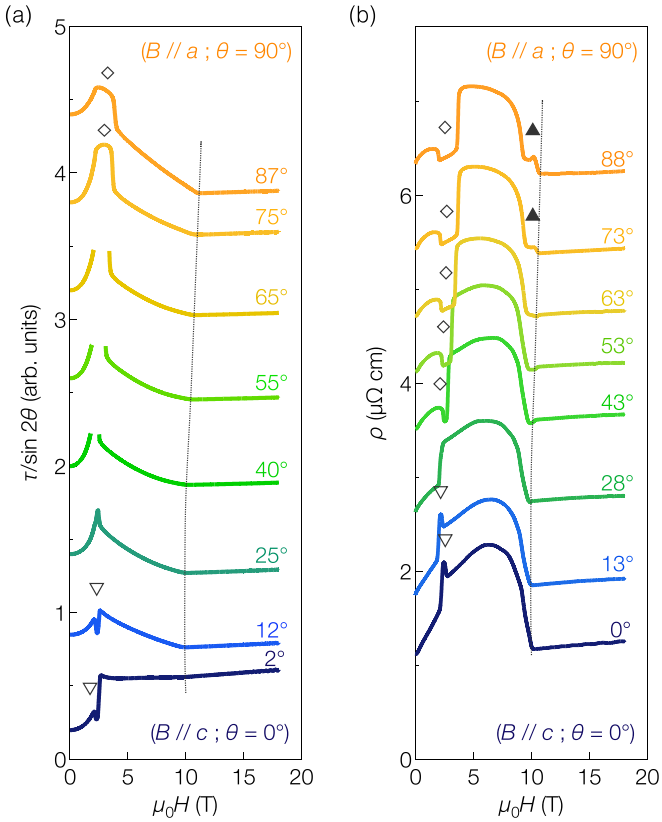

FIG. 4. Angular dependence of (a) magnetic torque and (b) magnetoresistance at $T = 1.3$ K. The data are shown only for selected angles with constant shifts for clarity.

are out of the measurement range. The dip in τ and hump in ρ, which correspond to phase II, are observed around $\theta = 0^\circ$ (open inverted triangle). They vanish when the field direction is tilted more than $\theta \sim 25^\circ$. The application of the tilted magnetic field with $\theta > 40^\circ$ results in the appearance of another steplike feature in both τ and ρ (open diamonds). These features suggest the disappearance of the SkL phase and stabilization of a different magnetic phase for the tilted field directions. When the field is applied in the vicinity of the a axis ($\theta > 70^\circ$), an additional hump structure appears only in the magnetoresistance (solid triangles), which also indicates the appearance of another magnetic phase just below the saturation field. The high-field phase is not detected in the torque measurements, which may imply similar magnetic anisotropies for these adjacent phases. The angular dependence of the B-T phase diagram was reported in Ref. [19], which is consistent with our observations.

The dHvA oscillations are clearly observed in the FF phase regardless of the field direction, while the dHvA oscillations in phase III and SdH oscillations in the FF phase are observed in the limited angle range. Figures 5(a) and 5(b) show the angular dependences of the normalized FFT spectra of dHvA and SdH oscillations in the FF phase, respectively. Peak positions in the FFT spectra are plotted as a function of the field angle θ in Figs. 5(c) and 5(d). The dashed curves drawn in Fig. 5(c) are to guide the eye, and several branches can be identified. The F_S peaks observed in SdH oscillations [shown as solid symbols in Fig. 5(d)] are seen only in the 3° range from the c axis. This might be because of the quasi-two-dimensional crystal structure of this sample: Gd magnetic layers are sandwiched between two (Ru, Si) blocks. When the

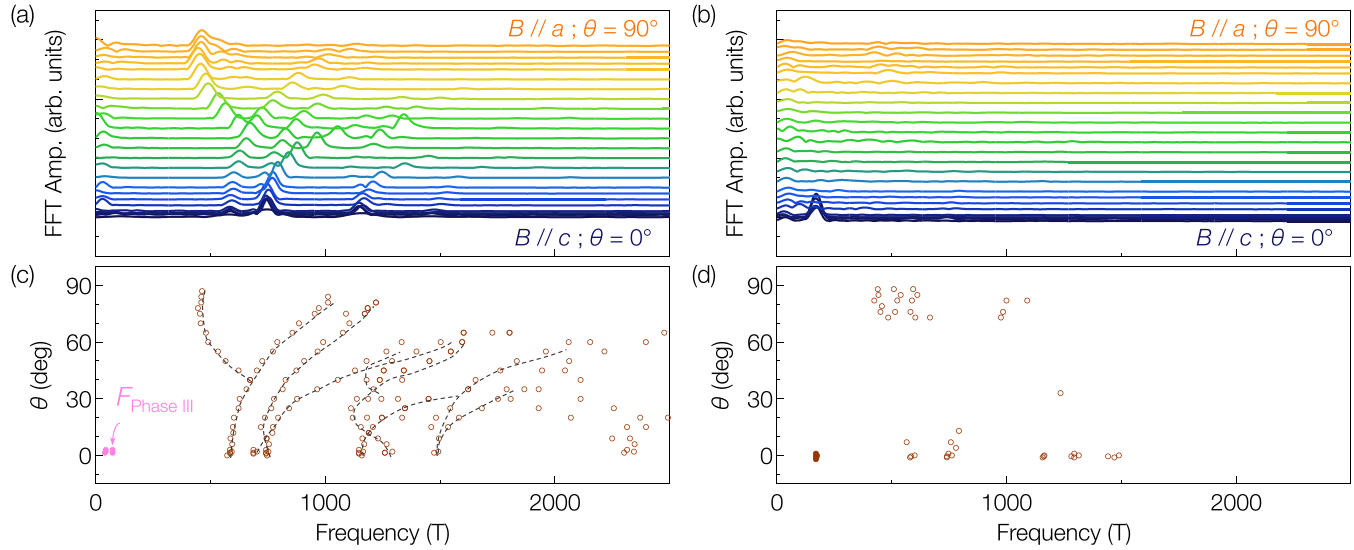

FIG. 5. Angular dependence of the (a) dHvA and (b) SdH oscillations in the FF phase. The peak positions of the spectra are plotted in (c) and (d), respectively.

field is tilted away from the c axis, the scattering probability in the cyclotron orbit may be enhanced with a stacking fault.

The dHvA oscillation in phase III also appears only in the narrow-angle range $|\theta| < 3°$, as shown by pink dots in Fig. 5(c). According to a previous study [19], the phase boundary does not change by 3° tilting, indicating that the disappearance of the dHvA is not related to any magnetic phase transition. Alternatively, we propose that the weak out-of-plane spin correlation due to the quasi-two-dimensional structure accounts for the disappearance of the quantum oscillation in the tilted field direction. The weak spin correlation between the layers may result in an irregular phase change in the spin modulation across the layers. This increases the scattering probability for interlayer conduction and could lead to a sudden reduction of the quantum oscillation magnitude when the field direction is tilted. Indeed, the weak spin coupling was suggested by a theoretical study [34].

C. Torque measurement under pulsed magnetic fields

The field dependences of magnetic torque measured in pulsed fields up to 58 T are shown in Fig. 6(a). At ~56 T, another high-frequency oscillation starts [Fig. 6(c)], which is not observed in the data up to 18 T. For the data taken at $\theta = 85°$ in Fig. 6(a), the high-frequency oscillation is observed above ~50 T, with the lower-frequency one observed in the steady-field experiment. Here, we focus on the high-frequency oscillation which is observed only in the pulsed-field experiments [Fig. 6(b)]. To extract the high-frequency oscillations, we subtract the smooth background obtained with a cubic polynomial fit [dashed pink curve in Figs. 6(b) and 6(c)] from each of the high-field τ data sets. The oscillatory components of the high-frequency oscillation and FFT spectrum are shown in Fig. 6(d) and its inset. Because $\tau(B)$ for $\theta = 85°$ contains a large number of oscillations, a sharp double-peak structure centered at ~15000 T is resolved, as seen in the inset of Fig. 6(d). The origin of this fine structure is considered to be the spin-split bands, which will be discussed later. As seen in the inset of Fig. 6(d), the low-frequency oscillation also induces a broad peak structure at about 1200 T, which is not well resolved due to the limited field window used for the FFT. In contrast to the data for $\theta = 85°$, $\tau(B)$ for the other angles shows a too small number of oscillations to resolve the fine structure of the FFT peak.

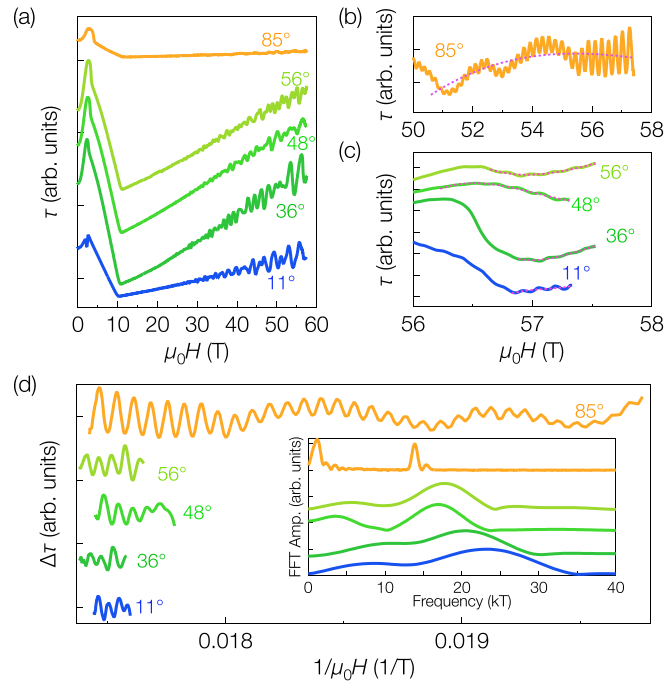

FIG. 6. (a) Field dependence of the magnetic torque of $GdRu_2Si_2$ using a pulsed field up to 58 T with constant shifts. (b) and (c) Expanded view of the high-field region in (a). Subtracted backgrounds for each data set are shown by pink dotted lines. (d) The oscillatory components of the high-frequency dHvA oscillations and the FFT spectra of the dHvA oscillations (inset), both shifted for clarity.

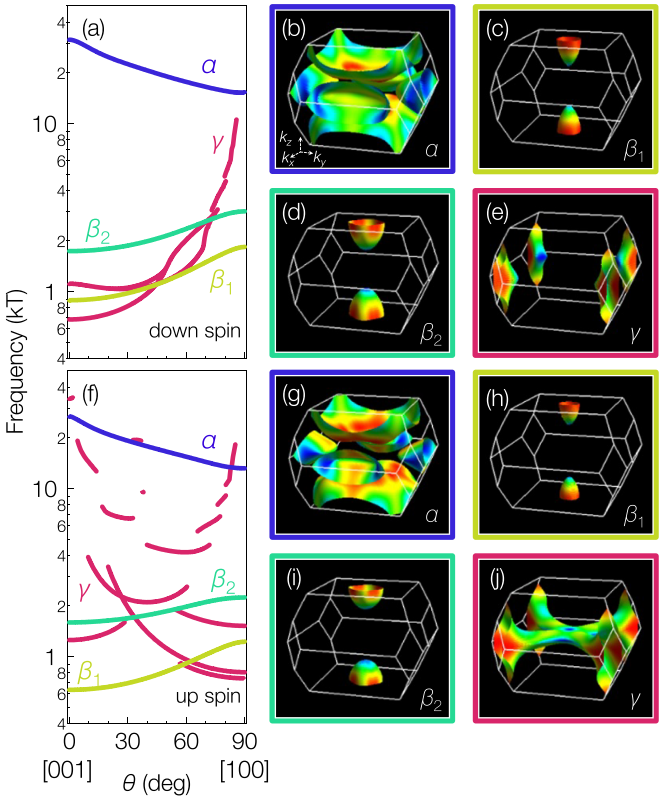

FIG. 7. (a) and (f) Calculated frequencies of the dHvA oscillations for $GdRu_2Si_2$ as a function of the magnetic field direction. Fermi surfaces for (b)–(e) the down spin and (g)–(j) the up spin drawn by the FERMISURFER code [46]. α and $\beta_{1,2}$ are hole sheets, while γ is an electron sheet.

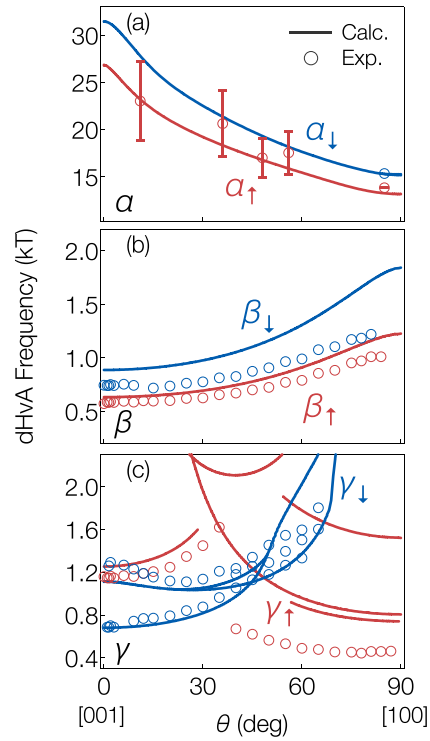

FIG. 8. Angular dependence of the dHvA oscillation frequencies for (a) the α band, (b) the β band, and (c) the γ band.

D. Theoretical calculation

The calculated Fermi surfaces and the angular dependences of the quantum oscillations are shown in Fig. 7. Four Fermi surfaces are expected for each spin-up and spin-down band. One large hole surface termed α and two small hole pockets termed $\beta_{1,2}$ are centered at the Z point. In addition, one electron pocket termed γ is predicted. Note that the topology of the γ surfaces depends on its spin states because of the large spin polarization. The density of states around the zone center exists only for the spin-up band [Fig. 7(j)]. In contrast, the pillarlike parts at the corners are split into two Fermi surfaces for the spin-up and spin-down bands [Figs. 7(e) and 7(j)].

The calculation predicts that the topology of the γ surface of the up spins changes when the Fermi energy is shifted by 50 meV. A hole emerges at the zone center, where the Fermi surface changes from an ellipsoidal sphere to a torus by shifting the Fermi energy. Similar behavior is also predicted for the non-f reference material $LaRu_2Si_2$ [47,48].

IV. DISCUSSION

A. Fermi surfaces of $GdRu_2Si_2$

Here, to clarify the electronic structure in the FF phase, we compare the angular dependence of the calculated oscillation frequencies with that of dHvA oscillations, which are observed throughout the angle range.

We identify six branches: one electron sheet and two hole sheets (three for each spin-split subband). In Fig. 8, the calculated FFT frequencies (solid lines) are plotted with the experimental data (circles). First, the calculated angle dependence of the large hole surface (α) shows good agreement with the angular dependence of the high-frequency oscillation detected in the pulsed magnetic fields. The splitting width of the double-peak structure resolved for $\theta = 85^\circ$ is consistent with the frequency difference in the calculated spin-up and -down branches [Fig. 8(a)], although the large error for $\theta < 85^\circ$ hinders tracking the angular dependence of the spin splitting. Next, we find that the angular dependences of F_1 and F_2 resemble the calculated angular dependences for the spin-split ellipsoidal hole surface β, as seen in Fig. 8(b). The slight discrepancy between the experimental and theoretical results is the number of Fermi surfaces. The present calculation predicts four fundamental oscillations originating from the two spin-split pairs of ellipsoidal hole surfaces $\beta_{1,2}$, while the torque magnetometry detects only two dHvA oscillations originating from one spin-split pair of β_1. The difference in the number of the ellipsoidal hole surfaces β was also discussed in several calculation studies for $LaRu_2Si_2$, $CeRu_2Si_2$ [47–49], and another $ThCr_2Si_2$-type material [50]. According to these studies, the number of sheets β are sensitive to the Fermi energy and the Wyckoff parameter of Si atoms. Thus, a detailed investigation of the lattice parameters at low temperatures, e.g., with diffraction experiments, might help to improve the accuracy of the ellipsoidal sheets β. Last, the FFT frequencies, including F_3, are found to be consistent with the angular dependence of the calculated angular dependence for the electron sheets γ, as shown in Fig. 8(c). In summary,

although there is a slight difference in the number of hole sheets β, experimental data are qualitatively reproduced by the calculated band structures.

Next, we discuss the SdH oscillation observed with $F_S = 176\,\mathrm{T}$, which is not observed in the dHvA oscillations. Such a different sensitivity of thermodynamic and transport probes or of different transport probes on the quantum oscillation was reported in earlier works [51,52]. The SdH oscillation at $F_S = 176\,\mathrm{T}$ might be related to the γ surface of the up spins $\gamma_\uparrow$ [Fig. 7(j)]. The electronic structure of this band varies with a slight shift in the Fermi level, and it can be either an ellipsoidal sphere or a torus. When this Fermi surface becomes a torus, the quantum oscillation corresponding to the inner core of the torus can appear, which is a candidate for the F_S branch. In contrast to the transport probes sensitive to both the variation of the density of states and the change in the scattering time, the thermodynamic probes are sensitive to only the variation of the density of states [53]. Thus, the small cross section of the inner core might have only a small effect on the density of states and might show a negligibly small dHvA oscillation, although it can affect the scattering time, which results in a larger SdH oscillation.

Another possible explanation is the quantum interference effect, which is not due to Landau quantization and instead results from electrons on different trajectories [54,55]. This effect causes an oscillation only in resistivity and not in other thermodynamic properties, as is the present case. The amplitude of this oscillation, however, is known to be insensitive to variations in temperature [56,57]. This is in contrast to the observed oscillation of the F_S branch. A similar difference between dHvA and SdH oscillations is also reported for $CeAgSb_2$ [58]. In this quasi-two-dimensional $4f$-localized ferromagnet, the electronic structure has been investigated using both dHvA [59] and SdH [58,60,61] effects. According to the SdH investigation, the main peak was found at 25 T, which had not been reported in the dHvA experiment or predicted by the first-principles calculation. Furthermore, this SdH oscillation is sensitive to the field direction and strongly suppressed when the field is tilted more than 7° away from the c axis, while the dHvA oscillations are observed regardless of the field direction. These features are discussed in terms of field-orientation-sensitive scattering due to the magnetic anisotropy, the dimensionality of the Fermi surface, and quantum interference [58].

B. Comparison with $LaRu_2Si_2$

Here, the observed Fermi surfaces in $GdRu_2Si_2$ are compared with those of the non-f reference material $LaRu_2Si_2$ [47,62,63]. Tables II and III compare the observed dHvA frequencies and corresponding cyclotron masses in the two materials for $B \parallel c$ and $B \parallel a$, respectively. Note that the temperature dependence of dHvA was investigated with the field angle $\theta = 2°$ [Figs. 3(a) and 3(d)], which is adopted in Table II. In $LaRu_2Si_2$, a large hole sheet, two small hole ellipsoidal sheets, and one electron sheet are experimentally reported. The overall electronic structures of both compounds are almost the same and consist of α, β, and γ, although the number of hole ellipsoidal sheets β is different between $GdRu_2Si_2$ (one each for spin up $\beta_\uparrow$ and down $\beta_\downarrow$) and $LaRu_2Si_2$ (two spin-degenerate bands β_1 and β_2). The major difference between $GdRu_2Si_2$ and $LaRu_2Si_2$ is the spin polarization in the γ band in the FF state. The dHvA frequencies and effective masses for the α, β, and γ sheets in $GdRu_2Si_2$ are close to those reported in $LaRu_2Si_2$, as shown in Tables II and III. The effective masses of $LaRu_2Si_2$ and $GdRu_2Si_2$ are on the order of $0.1m_0 - 1m_0$ and much smaller than that of the typical heavy-fermion system $CeRu_2Si_2$, in which heavy carriers with an effective mass of $>100m_0$ were observed [64]. The light effective mass of $GdRu_2Si_2$ indicates that the $4f$ band is far below the Fermi level, which is consistent with the fact that the magnetization saturates at $7\mu_B$ per Gd^{3+} above 10 T [see Fig. 2(a)]. The band calculation indeed predicts that the $4f$ band is located ~4 eV below the Fermi energy [34].

TABLE II. Observed dHvA frequencies and corresponding cyclotron masses in $GdRu_2Si_2$ and $LaRu_2Si_2$ ($B \parallel c$).

$LaRu_2Si_2$ [62]			$GdRu_2Si_2$		
Band	F (kT)	m^*/m_0	Band	F (kT)	m^*/m_0
α	27.2	2.37	$\alpha_\uparrow$ $\alpha_\downarrow$		
β_1	0.86	0.55	$\beta_\uparrow$ $\beta_\downarrow$	0.56 0.76	0.30
β_2	1.35	0.67			
γ	0.65	0.51	$\gamma_\uparrow$ $\gamma_\downarrow$	0.76 1.16	0.55 0.58

C. Magnetic interactions in $GdRu_2Si_2$

Several theoretical frameworks have succeeded in reproducing the topological spin textures in centrosymmetric metal systems taking different magnetic interactions into account [22–34]. Here, based on the experimental results shown above, major magnetic interactions in this system are discussed.

First, we point out the significance of the RKKY interaction, the itinerant-electron-mediated interaction, in $GdRu_2Si_2$. According to the previous STM observation, different patterns in the local density of states were observed in each phase, reflecting the underlying magnetic structures [21]. This indicates that the electronic band structure can be modified

TABLE III. Observed dHvA frequencies and corresponding cyclotron masses in $GdRu_2Si_2$ and $LaRu_2Si_2$ ($B \parallel a$).

$LaRu_2Si_2$ [62]			$GdRu_2Si_2$		
Band	F (kT)	m^*/m_0	Band	F (kT)	m^*/m_0
α	13.0	1.44	$\alpha_\uparrow$ $\alpha_\downarrow$	13.8 15.3	
β_1	1.43	0.53	$\beta_\uparrow$ $\beta_\downarrow$	1.14 1.29	
β_2	2.12	0.84			
γ	0.75	0.47	$\gamma_\uparrow$ $\gamma_\downarrow$	0.46	

due to the different spin textures via the exchange interaction between the local moments and itinerant electrons. The modification of the band structure may change the quantum oscillation frequencies, which is consistent with our observation of the change in dHvA frequencies at the transition from phase III to the FF phase (Fig. 2). The modulation of the deeply localized Gd $4f$ spins can change the modulation pattern of the itinerant electrons at the Fermi level via the RKKY interaction.

On the one hand, the first-principles calculation study suggested that Fermi surface nesting in $GdRu_2Si_2$ enhances the RKKY interaction that stabilizes the helical modulation along the nesting vector [33]. The study predicted a barrel-shaped nested Fermi surface located around the zone center, whose nesting vector matches the experimentally observed magnetic modulation $\mathbf{Q} = (0.22, 0, 0)$. Although we do find a barrel-shaped sheet (pillarlike part of the γ band), it resides at the zone corner. The predicted nesting period, however, shows good agreement with the radius of the band β. Assuming a circular cross section, the magnetic modulation $\mathbf{Q} = (0.22, 0, 0)$ corresponds to the cross section whose radius is $k \sim 0.17\,\text{Å}^{-1}$. This is close to the estimated Fermi wave vectors of band β in the FF phase (0.13 and 0.15 Å^{-1}, respectively; Table I). The fair agreement with the experimental value might indicate that the helimagnetic modulation can be enhanced by the Fermi surface effect in $GdRu_2Si_2$.

We also comment on the interorbital frustration mechanism proposed by another first-principles calculation study [34]. This study started with the band structure calculation assuming the ferromagnetic background and obtained $J(\mathbf{Q})$, which was then decomposed into each atomic component. Although we cannot discuss the mechanism they proposed using our experimental results, the agreement between the present experimental results and theoretical calculation strongly indicates the plausibility of the calculated electronic structures presented in Ref. [34].

V. CONCLUSION

In this paper, we performed magnetic torque and magnetoresistance measurements on the centrosymmetric skyrmion host $GdRu_2Si_2$. We observed dHvA oscillations in both phase III and the FF phase and SdH oscillations in the FF phase. The angular dependence of the dHvA in the FF phase is qualitatively reproduced by the band structure calculation. This indicates that the previous *ab initio* calculation [34] captures well the electronic structure and magnetic interaction in this system.

Fermi surface reconstruction was also observed as a change in the dHvA oscillation frequency, reflecting the coupling between conduction electrons and localized spins. This confirms the significance of the RKKY interaction in $GdRu_2Si_2$. The Fermi wave vectors corresponding to the β surface detected by the dHvA oscillations in the FF phase are almost the same as the wave vector of magnetic modulation, as predicted by another microscopic calculation [33]. This agreement might suggest Fermi surface nesting, stabilizing the magnetic modulation characterized by the nesting vector with the RKKY interaction.

As we mentioned in the previous section, the Fermi surface reconstruction might occur at every magnetic phase transition. Thus, the electronic structures in the SkL phase (phase II) might deviate from those of phase III and the FF phase. Indeed, the real-space observation of conduction electrons by the STM experiment revealed the different patterns in the local density of states corresponding to each magnetic phase from phase I to III and the FF phase [21]. As a probe to investigate electronic structure, angle-resolved photoemission spectroscopy is one of the most powerful techniques and was recently conducted, unveiling the electronic structure of phase I [65]. However, the measurement can usually be conducted only at zero field, and the electronic structure of phase II is left for future research.

ACKNOWLEDGMENTS

The author thanks T.-H. Arima., S. Hayami, K. Ishizaka, and Y. Yasui for the insightful discussions. This work was partly supported by JSPS KAKENHI Grants-in-Aid for Scientific Research (Grants No. 19H05825, No. 20K14403, No. 20K20892, No. 21H04437, No. 21H04990, No. 21H05470, No. 21K13873, No. 21K13876, and No. 22H00104) and JST PRESTO (Grants No. JPMJPR20B4 and No. JPMJPR20L7). N.M. thanks the World-leading Innovative Graduate Study Program for Materials Research, Information, and Technology (MERIT-WINGS) for support.

[1] U. K. Rößler, A. N. Bogdanov, and C. Pfleiderer, Spontaneous skyrmion ground states in magnetic metals, Nature (London) **442**, 797 (2006).

[2] S. Mühlbauer, B. Binz, F. Jonietz, C. Pfleiderer, A. Rosch, A. Neubauer, R. Georgii, and P. Böni, Skyrmion lattice in a chiral magnet, Science **323**, 915 (2009).

[3] X. Z. Yu, Y. Onose, N. Kanazawa, J. H. Park, J. H. Han, Y. Matsui, N. Nagaosa, and Y. Tokura, Real-space observation of a two-dimensional skyrmion crystal, Nature (London) **465**, 901 (2010).

[4] S. Seki, X. Z. Yu, S. Ishiwata, and Y. Tokura, Observation of skyrmions in a multiferroic material, Science **336**, 198 (2012).

[5] Y. Tokunaga, X. Z. Yu, J. S. White, H. M. Rønnow, D. Morikawa, Y. Taguchi, and Y. Tokura, A new class of chiral materials hosting magnetic skyrmions beyond room temperature, Nat. Commun. **6**, 7638 (2015).

[6] I. Kézsmárki, S. Bordács, P. Milde, E. Neuber, L. M. Eng, J. S. White, H. M. Rønnow, C. D. Dewhurst, M. Mochizuki, K. Yanai, H. Nakamura, D. Ehlers, V. Tsurkan, and A. Loidl, Néel-type skyrmion lattice with confined orientation in the polar magnetic semiconductor GaV_4S_8, Nat. Mater. **14**, 1116 (2015).

[7] N. Kanazawa, S. Seki, and Y. Tokura, Noncentrosymmetric magnets hosting magnetic skyrmions, Adv. Mater. **29**, 1603227 (2017).

[8] A. Fert, N. Reyren, and V. Cros, Magnetic skyrmions: Advances in physics and potential applications, Nat. Rev. Mater. **2**, 17031 (2017).

[9] T. Kurumaji, T. Nakajima, M. Hirschberger, A. Kikkawa, Y. Yamasaki, H. Sagayama, H. Nakao, Y. Taguchi, T. hisa Arima, and Y. Tokura, Skyrmion lattice with a giant topological Hall effect in a frustrated triangular-lattice magnet, Science **365**, 914 (2019).

[10] M. Hirschberger, T. Nakajima, S. Gao, L. Peng, A. Kikkawa, T. Kurumaji, M. Kriener, Y. Yamasaki, H. Sagayama, H. Nakao, K. Ohishi, K. Kakurai, Y. Taguchi, X. Yu, T.-H. Arima, and Y. Tokura, Skyrmion phase and competing magnetic orders on a breathing kagomé lattice, Nat. Commun. **10**, 5831 (2019).

[11] N. D. Khanh, T. Nakajima, X. Yu, S. Gao, K. Shibata, M. Hirschberger, Y. Yamasaki, H. Sagayama, H. Nakao, L. Peng, K. Nakajima, R. Takagi, T.-H. Arima, Y. Tokura, and S. Seki, Nanometric square skyrmion lattice in a centrosymmetric tetragonal magnet, Nat. Nanotechnol. **15**, 444 (2020).

[12] R. Takagi, N. Matsuyama, V. Ukleev, L. Yu, J. S. White, S. Francoual, J. R. L. Mardegan, S. Hayami, H. Saito, K. Kaneko, K. Ohishi, Y. Ōnuki, T.-H. Arima, Y. Tokura, T. Nakajima, and S. Seki, Square and rhombic lattices of magnetic skyrmions in a centrosymmetric binary compound, Nat. Commun. **13**, 1472 (2022).

[13] K. Hiebl, C. Horvath, P. Rogl, and M. Sienko, Magnetic properties and structural chemistry of ternary silicides (RE, Th, U) Ru_2Si_2 (RE = RARE EARTH), J. Magn. Magn. Mater. **37**, 287 (1983).

[14] M. Ślaski, A. Szytuła, J. Leciejewicz, and A. Zygmunt, Magnetic properties of $RERu_2Si_2$ (RE = Pr, Nd, Gd, Tb, Dy, Er) intermetallics, J. Magn. Magn. Mater. **46**, 114 (1984).

[15] G. Czjzek, V. Oestreich, H. Schmidt, K. Łąka, and K. Tomala, A study of compounds GdT_2Si_2 by Mössbauer spectroscopy and by bulk magnetization measurements, J. Magn. Magn. Mater. **79**, 42 (1989).

[16] A. Garnier, D. Gignoux, D. Schmitt, and T. Shigeoka, Giant magnetic anisotropy in tetragonal $GdRu_2Ge_2$ and $GdRu_2Si_2$, Phys. B (Amsterdam, Neth.) **222**, 80 (1996).

[17] T. Samanta, I. Das, and S. Banerjee, Comparative studies of magnetocaloric effect and magnetotransport behavior in $GdRu_2Si_2$ compound, J. Appl. Phys. **104**, 123901 (2008).

[18] A. Devishvili, Magnetic properties of Gd^{3+} based systems, Ph.D. thesis, University of Vienna, 2010.

[19] N. D. Khanh, T. Nakajima, S. Hayami, S. Gao, Y. Yamasaki, H. Sagayama, H. Nakao, R. Takagi, Y. Motome, Y. Tokura, T.-H. Arima, and S. Seki, Zoology of multiple-Q spin textures in a centrosymmetric tetragonal magnet with itinerant electrons, Adv. Sci. **9**, 2105452 (2022).

[20] J. Jensen and A. R. Mackintosh, *Rare Earth Magnetism* (Clarendon, Oxford, 1991).

[21] Y. Yasui, C. J. Butler, N. D. Khanh, S. Hayami, T. Nomoto, T. Hanaguri, Y. Motome, R. Arita, T.-H. Arima, Y. Tokura, and S. Seki, Imaging the coupling between itinerant electrons and localised moments in the centrosymmetric skyrmion magnet $GdRu_2Si_2$, Nat. Commun. **11**, 5925 (2020).

[22] Z. Wang, Y. Su, S.-Z. Lin, and C. D. Batista, Meron, skyrmion, and vortex crystals in centrosymmetric tetragonal magnets, Phys. Rev. B **103**, 104408 (2021).

[23] O. I. Utesov, Thermodynamically stable skyrmion lattice in a tetragonal frustrated antiferromagnet with dipolar interaction, Phys. Rev. B **103**, 064414 (2021).

[24] R. Yambe and S. Hayami, Skyrmion crystals in centrosymmetric itinerant magnets without horizontal mirror plane, Sci. Rep. **11**, 11184 (2021).

[25] Z. Wang, Y. Su, S.-Z. Lin, and C. D. Batista, Skyrmion Crystal from RKKY Interaction Mediated by 2D Electron Gas, Phys. Rev. Lett. **124**, 207201 (2020).

[26] K. Mitsumoto and H. Kawamura, Replica symmetry breaking in the RKKY skyrmion-crystal system, Phys. Rev. B **104**, 184432 (2021).

[27] I. Martin and C. D. Batista, Itinerant Electron-Driven Chiral Magnetic Ordering and Spontaneous Quantum Hall Effect in Triangular Lattice Models, Phys. Rev. Lett. **101**, 156402 (2008).

[28] Y. Akagi, M. Udagawa, and Y. Motome, Hidden Multiple-Spin Interactions as an Origin of Spin Scalar Chiral Order in Frustrated Kondo Lattice Models, Phys. Rev. Lett. **108**, 096401 (2012).

[29] R. Ozawa, S. Hayami, and Y. Motome, Zero-Field Skyrmions with a High Topological Number in Itinerant Magnets, Phys. Rev. Lett. **118**, 147205 (2017).

[30] S. Hayami, R. Ozawa, and Y. Motome, Effective bilinear-biquadratic model for noncoplanar ordering in itinerant magnets, Phys. Rev. B **95**, 224424 (2017).

[31] S. Hayami and Y. Motome, Square skyrmion crystal in centrosymmetric itinerant magnets, Phys. Rev. B **103**, 024439 (2021).

[32] S. Hayami and Y. Motome, Noncoplanar multiple-q spin textures by itinerant frustration: Effects of single-ion anisotropy and bond-dependent anisotropy, Phys. Rev. B **103**, 054422 (2021).

[33] J. Bouaziz, E. Mendive-Tapia, S. Blügel, and J. B. Staunton, Fermi-Surface Origin of Skyrmion Lattices in Centrosymmetric Rare-Earth Intermetallics, Phys. Rev. Lett. **128**, 157206 (2022).

[34] T. Nomoto, T. Koretsune, and R. Arita, Formation Mechanism of the Helical $\boldsymbol{Q}$ Structure in Gd-based Skyrmion Materials, Phys. Rev. Lett. **125**, 117204 (2020).

[35] K. Momma and F. Izumi, *VESTA3* for three-dimensional visualization of crystal, volumetric and morphology data, J. Appl. Crystallogr. **44**, 1272 (2011).

[36] E. Ohmichi and T. Osada, Torque magnetometry in pulsed magnetic fields with use of a commercial microcantilever, Rev. Sci. Instrum. **73**, 3022 (2002).

[37] J. M. Ok, C. I. Kwon, Y. Kohama, J. S. You, S. K. Park, J.-H. Kim, Y. J. Jo, E. S. Choi, K. Kindo, W. Kang, K.-S. Kim, E. G. Moon, A. Gurevich, and J. S. Kim, Observation of in-plane magnetic field induced phase transitions in FeSe, Phys. Rev. B **101**, 224509 (2020).

[38] G. Kresse and J. Furthmüller, Efficient iterative schemes for *ab initio* total-energy calculations using a plane-wave basis set, Phys. Rev. B **54**, 11169 (1996).

[39] G. Kresse and D. Joubert, From ultrasoft pseudopotentials to the projector augmented-wave method, Phys. Rev. B **59**, 1758 (1999).

[40] J. P. Perdew, K. Burke, and M. Ernzerhof, Generalized Gradient Approximation Made Simple, Phys. Rev. Lett. **77**, 3865 (1996).

[41] A. A. Mostofi, J. R. Yates, Y.-S. Lee, I. Souza, D. Vanderbilt, and N. Marzari, wannier90: A tool for obtaining maximally-localised Wannier functions, Comput. Phys. Commun. **178**, 685 (2008).

[42] G. Pizzi *et al.*, Wannier90 as a community code: New features and applications, J. Phys.: Condens. Matter **32**, 165902 (2020).
[43] P. M. C. Rourke and S. R. Julian, Numerical extraction of de Haas-van Alphen frequencies from calculated band energies, Comput. Phys. Commun. **183**, 324 (2012).
[44] D. Shoenberg, *Magnetic Oscillations in Metals* (Cambridge University Press, Cambridge, UK, 1984).
[45] G. P. Mikitik and Y. V. Sharlai, Manifestation of Berry's Phase in Metal Physics, Phys. Rev. Lett. **82**, 2147 (1999).
[46] M. Kawamura, Fermisurfer: Fermi-surface viewer providing multiple representation schemes, Comput. Phys. Commun. **239**, 197 (2019).
[47] M.-T. Suzuki and H. Harima, Change of Fermi surface topology in $CeRu_2Si_2$ studied by LSDA+U method, J. Phys. Soc. Jpn. **79**, 024705 (2010).
[48] M. A. Monge, M. Biasini, G. Ferro, M. Gemmi, G. Satta, S. Massidda, P. Lejay, and A. Continenza, Fermi surface study of $LaRu_2Si_2$ and of heavy-fermion $CeRu_2Si_2$ above the Kondo temperature, Phys. Rev. B **65**, 035114 (2002).
[49] E. K. R. Runge, R. C. Albers, N. E. Christensen, and G. E. Zwicknagl, Electronic structure of $CeRu_2Si_2$, Phys. Rev. B **51**, 10375 (1995).
[50] P. Reiss, P. M. C. Rourke, G. Zwicknagl, F. M. Grosche, and S. Friedemann, $LhRh_2Si_2$: Sensitivity of the Fermi surface to the Siz-position, Phys. Status Solidi B **250**, 498 (2013).
[51] E. Hassinger, G. Knebel, T. D. Matsuda, D. Aoki, V. Taufour, and J. Flouquet, Similarity of the Fermi Surface in the Hidden Order State and in the Antiferromagnetic State of URu_2Si_2, Phys. Rev. Lett. **105**, 216409 (2010).
[52] G. Bastien, A. Gourgout, D. Aoki, A. Pourret, I. Sheikin, G. Seyfarth, J. Flouquet, and G. Knebel, Lifshitz Transitions in the Ferromagnetic Superconductor UCoGe, Phys. Rev. Lett. **117**, 206401 (2016).
[53] A. Pantsulaya and A. Varlamov, Possibility of observation of giant oscillations of thermoelectric power in normal metal, Phys. Lett. A **136**, 317 (1989).
[54] R. W. Stark and C. B. Friedberg, Interfering electron quantum states in ultrapure magnesium, J. Low Temp. Phys. **14**, 111 (1974).
[55] R. W. Stark and R. Reifenberger, Comparison of theory and experiment for two regimes of quantum interference oscillations in the transverse magnetoresistance of pure magnesium, J. Low Temp. Phys. **26**, 819 (1977).
[56] R. W. Stark and C. B. Friedberg, Quantum Interference of Electron Waves in a Normal Metal, Phys. Rev. Lett. **26**, 556 (1971).
[57] C. S. A. Müller, T. Khouri, M. R. van Delft, S. Pezzini, Y.-T. Hsu, J. Ayres, M. Breitkreiz, L. M. Schoop, A. Carrington, N. E. Hussey, and S. Wiedmann, Determination of the Fermi surface and field-induced quasiparticle tunneling around the Dirac nodal loop in ZrSiS, Phys. Rev. Res. **2**, 023217 (2020).
[58] E. Jobiliong, J. S. Brooks, E. S. Choi, H. Lee, and Z. Fisk, Magnetization and electrical-transport investigation of the dense Kondo system $CeAgsb_2$, Phys. Rev. B **72**, 104428 (2005).
[59] Y. Inada, A. Thamizhavel, H. Yamagami, T. Takeuchi, Y. Sawai, S. Ikeda, H. Shishido, T. Okubo, M. Yamada, K. Sugiyama, N. Nakamura, T. Yamamoto, K. Kindo, T. Ebihara, A. Galatanu, E. Yamamoto, R. Settai, and Y. Ōnuki, An unusual hollow cylindrical Fermi surface of a quasi-two-dimensional compound $CeAgSb_2$, Philos. Mag. B **82**, 1867 (2002).
[60] R. Prozorov, M. D. Vannette, G. D. Samolyuk, S. A. Law, S. L. Bud'ko, and P. C. Canfield, Contactless measurements of Shubnikov-de Haas oscillations in the magnetically ordered state of $CeAgSb_2$ and $SmAgSb_2$ single crystals, Phys. Rev. B **75**, 014413 (2007).
[61] K. D. Myers, S. L. Bud'ko, V. P. Antropov, B. N. Harmon, P. C. Canfield, and A. H. Lacerda, de Haas–van Alphen and Shubnikov–de Haas oscillations in $RAgSb_2$ (R = Y, La-Nd, Sm), Phys. Rev. B **60**, 13371 (1999).
[62] Y. Ōnuki, I. Umehara, A. Keiko Albessard, T. Ebihara, and K. Satoh, Magnetoresistance and de Haas-van Alphen effect in $CeRu_2Si_2$ and $LaRu_2Si_2$, J. Phys. Soc. Jpn. **61**, 960 (1992).
[63] H. Yamagami and A. Hasegawa, Electronic structure and Fermi surface of $LaRu_2Si_2$, J. Phys. Soc. Jpn. **61**, 2388 (1992).
[64] H. Aoki, S. Uji, A. Keiko Albessard, and Y. Ōnuki, Observation of heavy electrons in $CeRu_2Si_2$ via the dHvA effect, J. Phys. Soc. Jpn. **61**, 3457 (1992).
[65] Y. Ohigashi and K. Ishizaka (private communication).